Optics & Laser Technology 192 (2025) 113675

Contents lists available at ScienceDirect

Optics and Laser Technology

journal homepage: www.elsevier.com/locate/optlastec

Full length article

A predictive model for burr formation in ultrafast laser ablation based on accumulated fluence

Ainhoa Guinea *, Andrea Aginagalde, Joseba Mendiguren, Eneko Saenz de Argandoña, Aitor Ayerdi, Wilson Tato, Alaitz Zabala

Mechanical and Industrial Production Department, Mondragon Unibertsitatea, Mondragon 20500, Spain

ARTICLE INFO

Keywords:
Ultrashort laser
Prediction model
Burr

ABSTRACT

Femtosecond lasers are powerful tools for precise surface texturing. They minimise the occurrence of heat-affected zones, which helps avoid surface defects such as burrs. However, the use of suboptimal parameters can still result in burr formation. Burr formation is critical in tribological applications, but its evolution has not been systematically characterised in the literature. Existing approaches typically rely on estimating the temperature reached by the material to assess the heat accumulation. However, this method has proven insufficient across a wide range of average laser powers and ablation geometries. This study introduces and validates a novel semi-empirical model that employs accumulated fluence, defined as the total accumulated energy per unit area, as an indicator that is independent of power and geometry. This method highlights burr formation in multi-shot and line ablation. Comprehensive qualitative and quantitative analyses of burr evolution were conducted using height, area, and volume variables, which minimised the sensitivity to measurement artefacts. Based on the geometrical features of the generated burrs, three burr regimes were identified for dimples and two for lines. Despite the differences in burr evolution, a shared burr formation threshold was identified at an accumulated fluence of 92 J/cm^2 for 316L stainless steel. The proposed indicator enables the cost-effective calibration of a burr-free laser processing parameter window. The new indicator can be integrated into laser parameter prediction models to optimise the process design and facilitate the industrial applicability of femtosecond laser technology.

1. Introduction

Femtosecond lasers are a high-precision technology used to generate surface textures for various applications. These include improving tribological behaviour [1], creating antiviral and bactericidal surfaces [2], and altering optical properties [3]. The main characteristic of femtosecond lasers is their extremely short pulse duration, which is comparable to the thermal relaxation time of various materials. This enables the removal of material from the surface before heat diffuses through the lattice, which minimises the heat-affected zone (HAZ). In addition, femtosecond laser is a versatile technology, as the ultrashort pulse duration enables a high-intensity concentration that allows the ablation of almost any material, even at low power levels [4]. Femtosecond lasers are considered a green technology due to the absence of harmful coolants and acids as well as their contactless material removal, which eliminates tool wear [5]. However, despite their many advantages, the industrial use of femtosecond lasers for texturing is limited by two factors: (i) the complexity of selecting appropriate laser process parameters [6] and (ii) its comparatively low production rate [7]. To enhance the productivity and shorten the processing times, strategies such as using high-energy pulses [8], high pulse frequencies, burst ablation, and multi-spot beams [9] can be employed. While these strategies accelerate the ablation process, they also increase the risk of heat accumulation due to increased pulse energy and/or pulse-to-pulse interactions.

Heat accumulation occurs because the energy of the beam that is below the fluence threshold (i.e. the minimum energy required to ablate the material) does not contribute to the ablation but instead heats the surrounding material [10]. If the residual heat is not dissipated before the next laser pulse, it impinges on the locally preheated workpiece, leading to heat accumulation. The degree of heat accumulation depends on both the material's properties (e.g., density, heat capacity, thermal

* Corresponding author.
E-mail address: aguinea@mondragon.edu (A. Guinea).

https://doi.org/10.1016/j.optlastec.2025.113675
Received 16 May 2025; Received in revised form 28 June 2025; Accepted 3 August 2025
Available online 14 August 2025

diffusivity, melting temperature, and reflectivity) [8] and the laser parameters. The laser's parameters include the fluence, pulse repetition rate, and scanning speed [11] as well as the scanning strategy [12], wavelength, and polarisation [13]. Furthermore, the laser–matter interaction process affects heat accumulation because pulse-to-pulse interactions can lead to plasma and particle shielding. This shielding can prevent the complete absorption of subsequent pulses, which influences the amount of accumulated heat [12]. Therefore, if incorrect processing parameters are used, a significant portion of the absorbed laser power is converted into heat rather than used for ablation. In extreme cases, this accumulated heat can raise the temperature high enough to melt the irradiated material, resulting in ultrafast laser welding of materials, as reviewed by Jia *et al.* [14]. In less extreme scenarios, heat accumulation can lead to oxidation [15,16], melting layers [11,17], a poor surface finish due to the formation of bumpy structures [18,19], and burr formation along the edges of laser surface textures [20,21].

Burr formation is particularly detrimental in tribological applications. In this context, burrs disrupt surface conformity, introduce stress concentrations, and extend the running-in period [22]. They can also increase the adhesion between contacting surfaces [23] and interfere with the formation of a lubrication film [24]. All of this can result in increased friction and wear, depending on the width, shape, and height of the burr [24]. The HAZ, defined as the region surrounding the texture perimeter where microstructural changes occur, is closely linked to burr formation. Kar *et al.* [25] drilled holes in grade 2 titanium and analysed the width of the HAZ through microscope image processing. In addition, the holes were measured with a 3D optical profilometer. The results revealed high burrs inside the HAZ. Similarly, Wei *et al.* [26] ablated lines in gallium nitride and measured them with a confocal microscope; material peaks inside the HAZ were observed. However, despite the critical importance of burr formation, no comprehensive study has systematically characterised the evolution of burrs across different laser processing conditions. Past studies have primarily relied on qualitative observations using scanning electron microscopy (SEM) [20] or have focused solely on the burrs' widths. The relationship between the heat accumulation and the burr height remains largely unexplored.

To analyse heat accumulation, the most common approach in the literature involves calculating the temperature reached by the material. It is generally assumed that maintaining a material temperature below a critical threshold is essential for preserving the surface quality [17]. Two primary modelling approaches have been used to predict the evolution of the material's temperature. (i) The Two-temperature model (TTM) is a system of coupled equations that describes the temporal and spatial evolution of the electron and lattice temperatures during and after pulse irradiation. This model provides a detailed understanding of the thermal dynamics in the material, allowing for the prediction of temperature profiles and heat accumulation [27]. Nevertheless, it has high computational demands, which are often not affordable for multi-pulse, line, or 2D area ablation. (ii) The heat conduction equation is another approach to calculate the temperature in the material. Analytical solutions to this equation are commonly employed, assuming instantaneous heat sources and constant material properties [21]. Numerical methods for solving the heat conduction equation can also be employed, which enable researchers to consider the heating phase and evolution of material properties along with the temperature. This approach provides a more accurate description of the behaviour of the system, but at a higher computational cost than analytical solutions [18,28].

Some studies have indicated that the temperature reached in the material alone is insufficient to predict defects caused by heat accumulation. For instance, Cangueiro *et al.* [12] demonstrated that the degree of oxidation in ablated stainless steel, aluminium, and copper did not correlate directly with computed temperature values. Similarly, Martan *et al.* [11] observed melted layers in laser-processed 304 steel, even when theoretical calculations indicated that the temperatures would be below the melting point. Chijiwa *et al.* [29] linked thermal damage to bumpy surface roughness; however, they noted that bumpy structures occurred even when critical temperatures were not exceeded. Moreover, Shin *et al.* [13] reported that high pulse frequencies, which increased the material's temperature, actually reduced the burr formation in Invar sheet processing, contrary to their expectations. Additionally, to the authors' knowledge, no prior study has established a direct relationship between the temperature reached in the material and the characteristics of the resulting burrs. Overall, the findings indicate that defect formation in femtosecond laser processing is governed by factors other than simple temperature thresholds.

Optimising processing parameters to achieve defect-free surfaces remains challenging due to the complex nature of laser-material interactions. Laser parameter prediction models are often based on logarithmic ablation laws [6] cannot account for defects arising from heat accumulation. To ensure the quality of generated surface textures, Holder *et al.* [30] employed a prediction model for high average power lasers, in which a minimum velocity was established for each pulse frequency. The assumption of a constant minimum velocity across all other processing parameters in this innovative approach offered practical simplicity; however, the same assumption limits the model's adaptability. This situation highlights the need for a robust and universally applicable indicator, whose value can be systematically defined, to establish optimal processing conditions and prevent burr formation and related defects.

Heat accumulation during femtosecond laser processing results in oxidation, melting layers, poor surface finish, and burrs at the edges of the texture. These problems compromise the quality and functionality of the surfaces. Among these challenges, burr formation and their related geometrical features (width, height, and shape) have a crucial impact on tribological performance. Despite the relevance, there is a lack of comprehensive studies on the geometric characterisation of the formation and growth of burrs under varying processing conditions. Furthermore, current approaches typically use the temperature reached in the material as an indicator of defect formation, but this method has proven insufficient when the average power fluctuates. This point highlights the need for a more reliable and predictive indicator for how defects emerge during laser texturing.

This study aims to establish a robust indicator to define the limits of laser processing parameters that ensure the generation of burr-free ultrafast laser textures. It also provides a detailed geometric characterisation of burr formation and growth; such information is helpful for developing a clear and objective criterion to identify burr-free textures. It should be noted that this study does not focus on the fundamental physical mechanisms that underlie burr generation due to heat accumulation. For detailed discussions on the physics of thermal effects in ultrafast laser processing, the reader is referred to [14]. Instead, this study introduces the accumulated fluence limit as a practical, geometry- and power-independent indicator of burr formation. The indicator can be used together with the proposed burr characterisation methodology and is readily integrated into existing laser process prediction models. It enhances the accuracy of those models and eliminates reliance on operator expertise while also reducing trial-and-error experimentation. This advancement facilitates a reliable process optimisation and supports the broad industrial application of femtosecond laser technology for high-quality surface texturing.

The remainder of this paper is organised as follows. First, two models for assessing the heat accumulation threshold are introduced: (i) an analytical heat-conduction model to calculate the temperature reached during laser processing, and (ii) the accumulated fluence profile model that is proposed in this study as a novel indicator of heat accumulation. Next, the materials and methods are described, with a focus on the burr characterisation procedure. Burr appearance and characteristics serve as indicators of heat accumulation. In the next section, the fit between actual burr formation and each of the proposed models is analysed and discussed; the aim is to establish a critical threshold for burr-free laser processing. Finally, the main conclusions of the study are summarised.

2. Models

This section presents two models used to assess the heat accumulation threshold. The first is an analytical heat conduction model, based on established formulations in the literature, which is employed to estimate the temperature reached during laser processing. The second is the accumulated fluence profile model, which this study proposes, where the accumulated fluence provides a novel and semi-empirical indicator of heat accumulation.

2.1. Analytical heat conduction model

The main model used in the literature to calculate the temperature reached by a material considers that a portion of the total incident pulse energy (E_p) is absorbed by the material. The absorbed energy that is not utilized to ablate the material (i.e. the energy below the energy threshold) remains as thermal energy [21]. Therefore, E_p can be elaborated as follows:

$$E_p = E_{ref} + E_{abl} + E_{th} \tag{1}$$

where E_{ref} is the reflected energy, E_{abl} is the energy used for material ablation, and E_{th} is the remaining thermal energy. The E_{ref}, E_{abl}, and E_{th} terms are complex and depend on (i) the material's properties (such as its thermal diffusivity, reflectivity, density, and heat capacity); (ii) the laser processing parameters (including E_p, the spatial and temporal profile of the pulse, the pulse frequency, and its speed); (iii) the actual geometry of the interaction zone (incident angle and multiple reflections); and (iv) the laser matter interaction process (particle and plasma shielding phenomena) [8]. In this study, the calculations are based on the assumption that E_{th} represents 28 % of the pulse energy (E_p), as described by Cangueiro *et al.* [12] for various metals.

Heat conduction through the material is analysed within the framework of classic thermodynamics, which neglects convection and radiation mechanisms [31]. Hence, the spatial and temporal evolution of the temperature field resulting from ultrashort laser ablation can be described by solving the heat conduction equation in semi-infinite and infinite bodies. It is assumed that E_{th} is concentrated in the most superficial layer of the surface within a timescale shorter than that required for heat to be conducted to the bulk. Since the heating phase is neglected, E_{th} is considered an instantaneous superficial point heat source [21]. Therefore, the temperature distribution for the surface layer after a single pulse (T_{single}) with a Gaussian beam profile is given by Equation (2) and Equation (3), [12]

$$T_{single}(x,y,t) = \frac{2E_{th}\boldsymbol{\Theta}(t-t_0)}{\pi\rho c_p(8\kappa(t-t_0)+\omega_0^2)\sqrt{\pi\kappa(t-t_0)}}e^{\varphi} \tag{2}$$

$$\varphi = \frac{(x-x_0)^2+(y-y_0)^2}{4\kappa(t-t_0)}\left(\frac{\omega_0^2}{8\kappa(t-t_0)+\omega_0^2}-1\right) \tag{3}$$

where ρ is the density, c_p is the heat capacity, κ is the thermal diffusivity, ω_0 is the spot size of the laser, x_0 and y_0 are the coordinates of the centre of the laser spot, and t_0 is the instant at which the laser pulse impinges the material. The Heaviside function ($\boldsymbol{\Theta}$) is equal to 0 for arguments $x < 0$ and equal to 1 for arguments $x \geq 0$. It should be noted that the thermophysical properties of the material are considered to be constants, regardless of the temperature attained.

For the solution of multi-shot dimples and line ablation, t_0 varies with the number of pulses (N), as described by Equation (4):

$$t_0(N) = \frac{(N-1)}{f} \tag{4}$$

where f is the pulse frequency. Moreover, in line ablation, x_0 varies with the number of pulses due to the laser beam movement, according to Equation (5):

$$x_0(N) = \frac{v\cdot(N-1)}{f} \tag{5}$$

where v is the speed of the laser. Hence, the total temperature profile is obtained by Equation (6):

$$T(x,y,t) = T_{room} + \sum_{N=1}^{N=N_p} T_{single}(x,y,t,N) \tag{6}$$

where N_p is the total number of incident pulses, and T_{room} is the room temperature. Based on this description of the model, Fig. 1 illustrates the predicted temperature evolution at the centre of a multi-shot ablated dimple and line, respectively. The figure highlights the effects of heat accumulation under repeated laser pulses. Each pulse leads to an instantaneous temperature rise, followed by a decay caused by the heat conduction. If the material does not cool down to T_{room} between pulses, the minimum temperature gradually rises and then reaches a steady state known as saturation temperature (T_{sat}). In the case of lines, an asymmetric temperature profile arises due to the movement of the heat source (see Fig. 1 (b)). The key indicator analysed in this study is the maximum saturation temperature [12].

2.2. Accumulated fluence profile model

The accumulated fluence profile model was first proposed by Eichstädt *et al.* [32] for predicting laser process parameters that would generate homogeneous laser-induced periodic surface structures (LIPSS). 'Fluence' refers to the laser irradiation energy per unit area. This model focuses on the amount and distribution of fluence that is transferred to the material, without considering any laser–matter interaction processes. Therefore, the calculation is independent of material properties. The fluence distribution for a focused single pulse of a Gaussian beam profile (F_{single}) is described by Equation (7) and Equation (8), as follows:

$$F_{single}(x,y) = \frac{2E_p}{\pi\omega_0^2}e^{\gamma} \tag{7}$$

$$\gamma = \left(-2\frac{(x-x_0)^2+(y-y_0)^2}{\omega_0^2}\right) \tag{8}$$

The fluence delivered by each incident pulse is superimposed. Consequently, the fluence profiles of each pulse are accumulated ($F_{accu}(x,y)$) according to Equation (9):

$$F_{accu}(x,y) = \sum_{N=1}^{N=N_p} F_{single}(x,y,N) \tag{9}$$

It should be noted that in the case of line ablation, x_0 varies with the number of pulses due to the laser movement, according to Equation (5).

To visualise the model's predictions, 2D representations of the generated accumulated fluence profile for dimples and lines are presented in Fig. 2. The accumulated fluence value (F_{accu}) is computed from the accumulated fluence profile ($F_{accu}(x,y)$) as the peak value for dimples (see Fig. 2 (a)) and as the mean value of the steady state in the centre for the lines (see Fig. 2 (b)).

3. Materials and methods

The experiments were conducted on a 316L stainless steel disc having a density of 7930 kg/m^3 and heat capacity of 472 J/kg K, with a thermal diffusivity of $3.9\cdot10^{-6}$ m^2/s. The 316L stainless steel type was selected because it is widely used in ultrafast laser studies. Furthermore, it has certain tribological applications, such as bearings and mechanical seals, for which laser surface texturing can improve the performance [1]. The disc (⌀50 x 4.7 mm) was polished sequentially using diamond

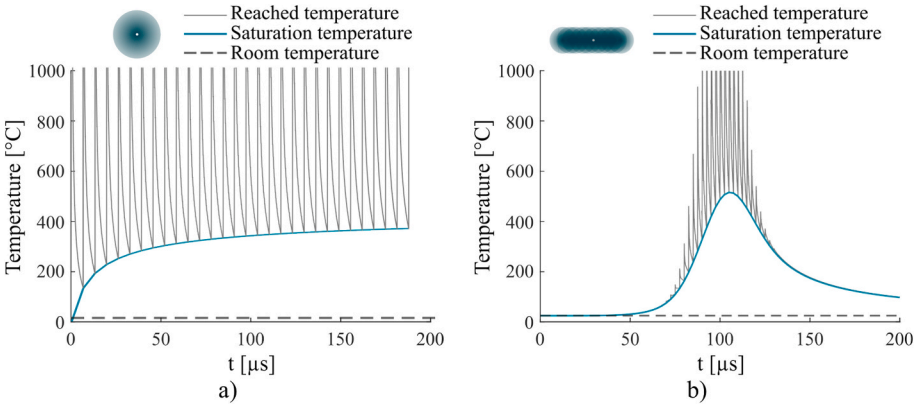

Fig. 1. Temporal evolution of the temperature in the top surface layer and centre of the laser radiation with a pulse frequency of 400 kHz and pulse energy of 3.6 µJ of (a) Multi-shot dimple with a burst time of 75 µs (b) Line with a speed of 500 mm/s.

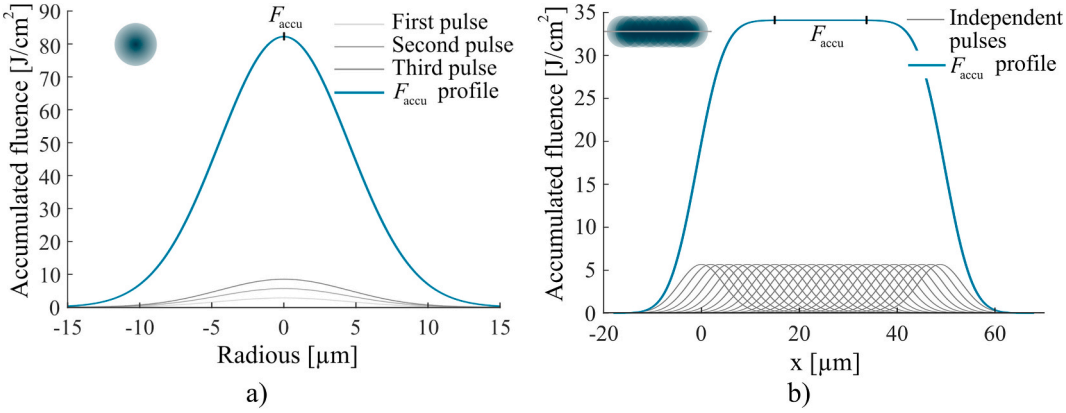

Fig. 2. Accumulated fluence profile with a pulse frequency of 400 kHz and pulse energy of 3.6 µJ of a) Multi-shot dimple with a burst time of 75 µs b) Line with a speed of 750 mm/s.

polishing powders of 6 µm and 1 µm. The resulting surface topography parameters after three measurements are shown in Table 1. The disc was cleaned with a lint-free WYPALL X70 cloth and acetone before the laser ablation. After laser processing, the disc was ultrasonically cleaned for 5 min at 30 °C using acetone to ensure the removal of all ablation particles before the characterisation was performed.

The laser processing system used in this study was an LS-lab from LASEA, which was equipped with a Satsuma HP femtosecond fibre laser source developed by Amplitude system. The laser source produced a Gaussian beam spatial profile at a central wavelength of 1030 nm. The maximum average power was 10 W, delivering a maximum energy per pulse of 20 µJ. An F-theta focusing lens with a focusing distance of 100 mm was used to focus the laser beam on the part. All tests were conducted under constant values for the wavelength, pulse duration, pulse repetition rate, and spot size, as listed in Table 2. These variables influence the ablation threshold and incubation behaviour of the material. The spot size was determined using the method established by Liu [33]. The polarisation was set to circular to minimise irregularities in the laser absorption.

Three repetitions of multi-shot dimple and line matrices were ablated using six different values for the number of pulses and speed, respectively; in addition, four peak fluence values were employed (see Table 2). This resulted in a total of 24 dimples or lines per experimental matrix. The speed values were selected to generate the same accumulated fluence for the line matrix as the multi-shot dimple matrix.

Table 1
Surface topography parameters of the polished stainless-steel disc.

Sa [µm]	Sq [µm]	Sz [µm]	Sp [µm]
0.007 ± 0.002	0.009 ± 0.003	0.111 ± 0.019	0.035 ± 0.002

Table 2
Summary of test conditions.

Wavelength [nm]	1030
Pulse duration [fs]	350
Pulse repetition rate [kHz]	400
Spot size [µm]	8.86*
Polarisation	Circular
Repetitions	3
Power [W]	0.17, 0.4, 0.96, 1.13
Peak fluence [J/cm²]	0.35, 0.807, 1.946, 2.286
Number of pulses (multi-shot dimple matrix)	10, 40, 70, 100, 130, 160
Speed [mm/s] (line matrix)	56, 69.5, 90, 128.5, 225, 900

* The spot size was determined through the D2 method [33].

Qualitative and quantitative analyses were performed regarding the generated burr. For the qualitative analysis, a FEI NOVA NANOSEM 450 scanning electron microscope was used. The images were captured under high vacuum conditions ($4.8 \cdot 10^{-4}$ Pa) in secondary electron (SE) mode, with an acceleration voltage of 20 kV and at working distance of 4.7 mm.

Quantitative analysis of the burr was performed using a Sensofar S-NEOX optical profilometer with confocal technology and EPI 100X objective (repeatability rsm < 4 nm and spatial sampling = 130 nm). The acquisition area was 490.97 x 131.83 µm^2. Post-processing of the acquired data was initially performed using SensoMap Premium 7.4

metrology software. The surface form was removed using a first-order polynomial fitting (F-operator), and noise was subtracted using a Gaussian filter with $\lambda s = 1.3$ µm (S-filter). The processed surface data (SF surface) were then exported to MATLAB 2023a for further analysis. Burr identification was performed by setting the S_p value of the reference surface as a threshold for surface cropping. Any surface features that exceeded this threshold were classified as burrs (see Fig. 3 (a)). For comprehensive characterisation, the burr volume as well as the projected area and the height were analysed.

The burr volume and projected area were quantified by summing the total volume and area, respectively, of all surface features that exceeded the S_p value of the reference surface (see Fig. 3 (b) and (c)). Regarding the height, the measured maximum height is notably sensitive to measurement artefacts such as spikes, which are narrow peaks that do not correspond to the actual surface topography. These artefacts can arise due to optical profilometry limitations or surface contamination. They lead to overestimated values, which reduce the robustness of the parameter for burr characterisation. To establish a more reliable height metric for Gaussian surfaces, Pawlus *et al.* [34] employed the material area ratio curve (Abbott-Firestone curve). They characterised the maximum surface height by truncating this ratio curve at a height that corresponded to three times the standard deviation of the surface height distribution (3σ). However, since the burr height distribution deviated from a Gaussian profile, this approach was not applicable in the current study. Instead, following the same idea, the burr height was defined at the 5 % material area ratio curve of the burr ($h_{0.05}$) to ensure a height parameter that was fairly representative and artifact-resistant (see Fig. 3 (d)).

In addition, the height profiles of the burrs were analysed. For dimples, a profile was extracted along the dimple perimeter (see Fig. 3 (e)). For lines, the profile along one perimeter edge parallel to the laser scanning direction was extracted (see Fig. 3 (f)).

4. Results and discussion

4.1. Saturation temperature

Saturation temperature was explored as a potential indicator for identifying the onset of burr formation. Fig. 4 (a), (b), and (c) illustrate the height, area, and volume, respectively, of the burrs that formed on dimples, as a function of T_{sat}. The marker shapes and colours represent differing levels of laser power. In Fig. 4 (a), the red horizontal line at 35 nm (S_p of the reference surface) serves as a height threshold indicator for the presence of burrs: data points above this threshold indicate significant burr formation, whereas those below indicate a lack of burrs. It should be noted that the analytical thermal model used in this study assumes fixed material properties and a constant absorption rate of 28 % for stainless steel, as commonly reported in the literature [12]. However, these assumptions were not experimentally validated under the specific processing conditions of this study due to the complexity of accurately measuring the temperature achieved by the material during ultrafast laser processing [11].

The data clustered into four groups corresponding to specific power levels. Within each power level, all burr dimensions (height, area, and volume) exhibited an exponential rise as T_{sat} increased. Additionally, a higher laser power amplified the differences in burr formation across different pulse numbers (N_p). This trend is attributed to the increasing variation in T_{sat} with N_p at higher power levels. For instance, at 0.14 W,

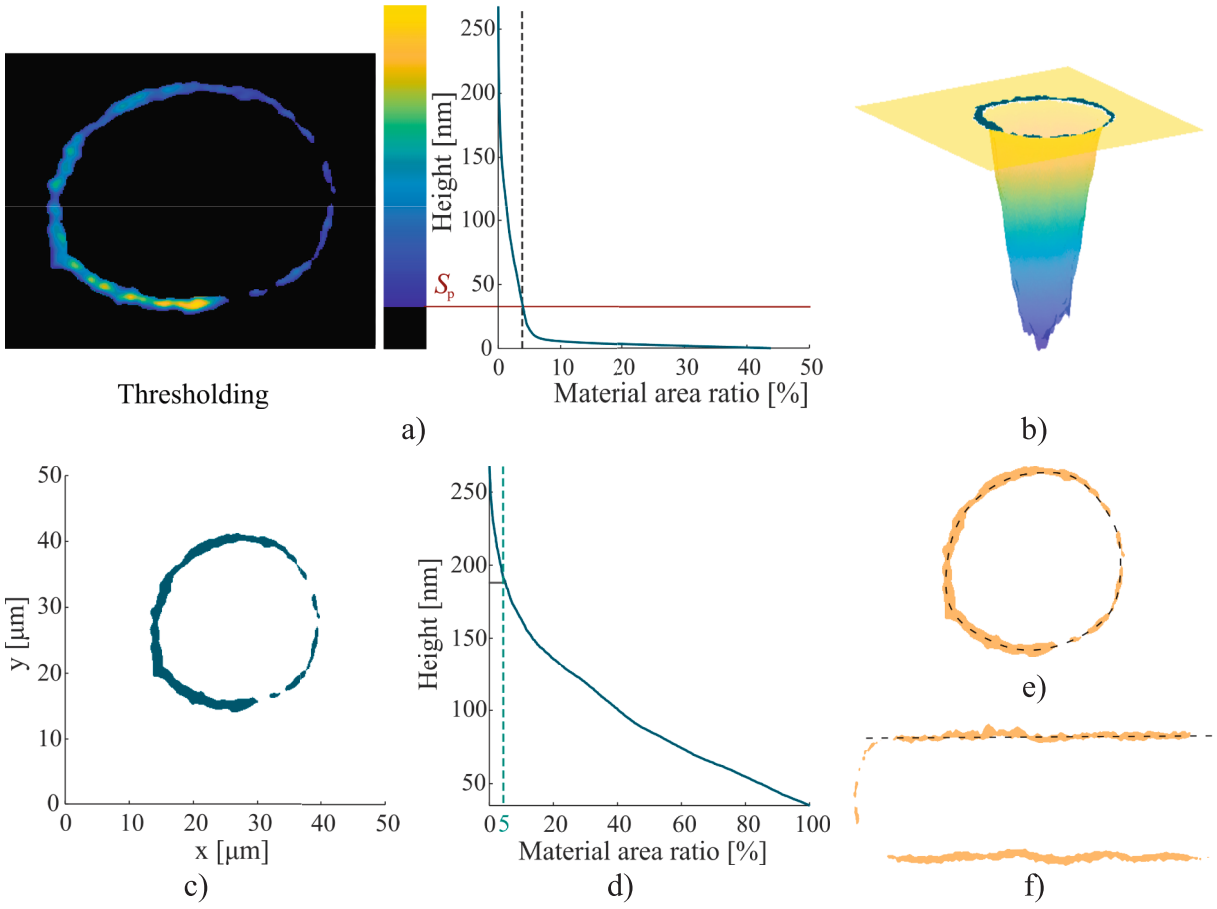

Fig. 3. Quantitative burr analysis: a) Thresholding technique for burr identification; b) Burr volume; c) Burr projected area; and d) Abbot-Firestone curve of the burr for height measures. Method for extracting profiles of the burr for e) Dimples and f) Lines. The dashed line in e) and f) represent the perimeter line.

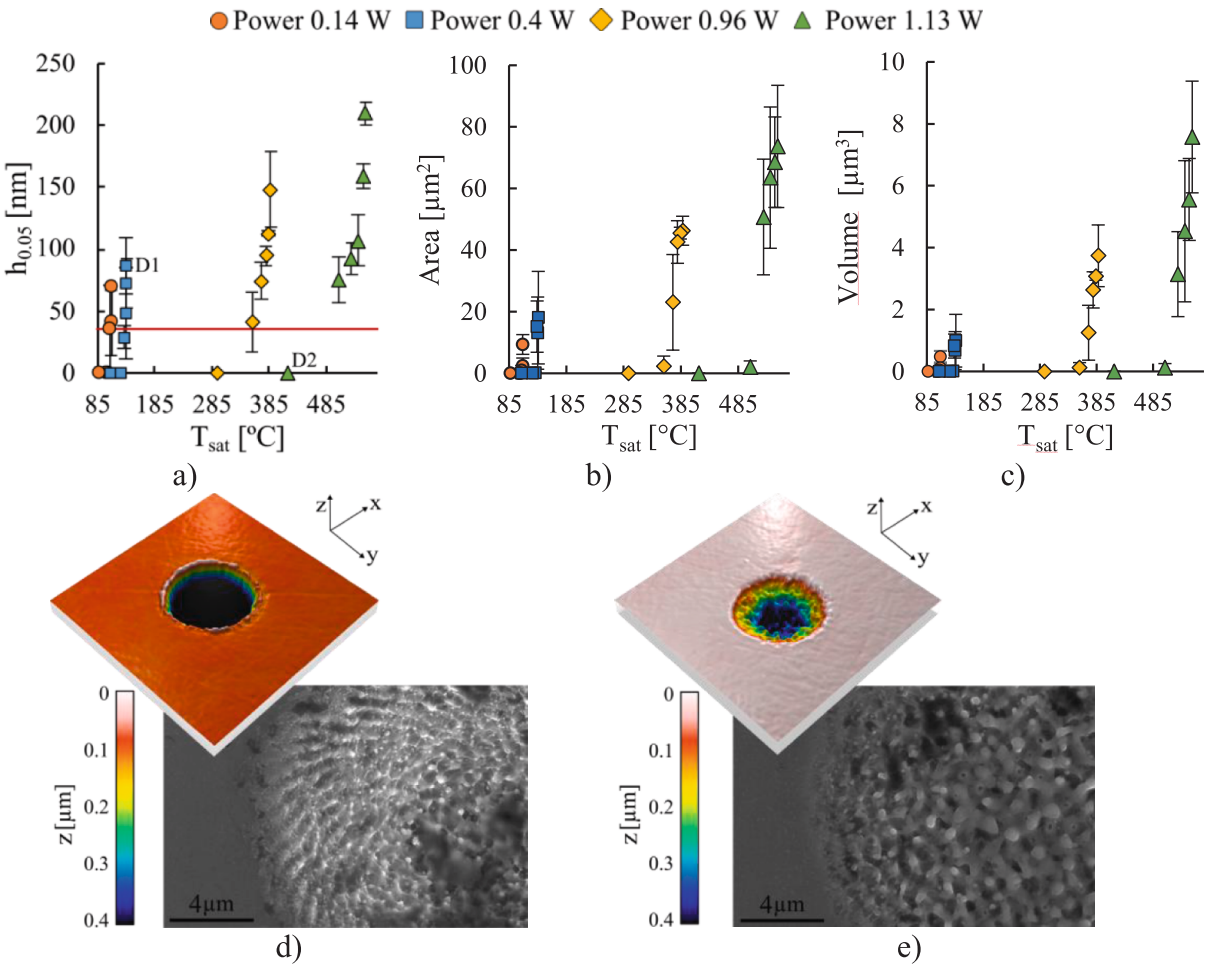

Fig. 4. Results for saturation temperature regarding burr in the multi-shot dimple. a) Height at 5 % of the material area ratio, with the red line representing the S_p value of the reference surface; b) projected area; c) volume, SEM and 3D measurements of d) dimple ablated using 0.4 W and 130 pulses, $T_{Sat} = 135\,^{\circ}C$ (D1) and e) dimple ablated using 1.13 W and 10 pulses, $T_{Sat} = 416\,^{\circ}C$ (D2).

the T_{sat} changed by only 22 °C when N_p was increased from 10 pulses to 160 pulses; in contrast, at 1.13 W, the temperature variation was 138 °C.

However, burr formation is not solely governed by T_{sat}, as evidenced by the differing behaviours observed at various power levels. At a laser power of 0.4 W, burrs formed when T_{sat} reached 135 °C (see Fig. 4 (a) and (d)). In contrast, at 1.13 W, no burrs were evident even when T_{sat} reached 416 °C (see Fig. 4 (a) and (e)). Therefore, a universal T_{sat} threshold for burr formation that is independent of laser power could not be established.

Burr formation on lines was then analysed. Fig. 5 (a), (b) and (c)

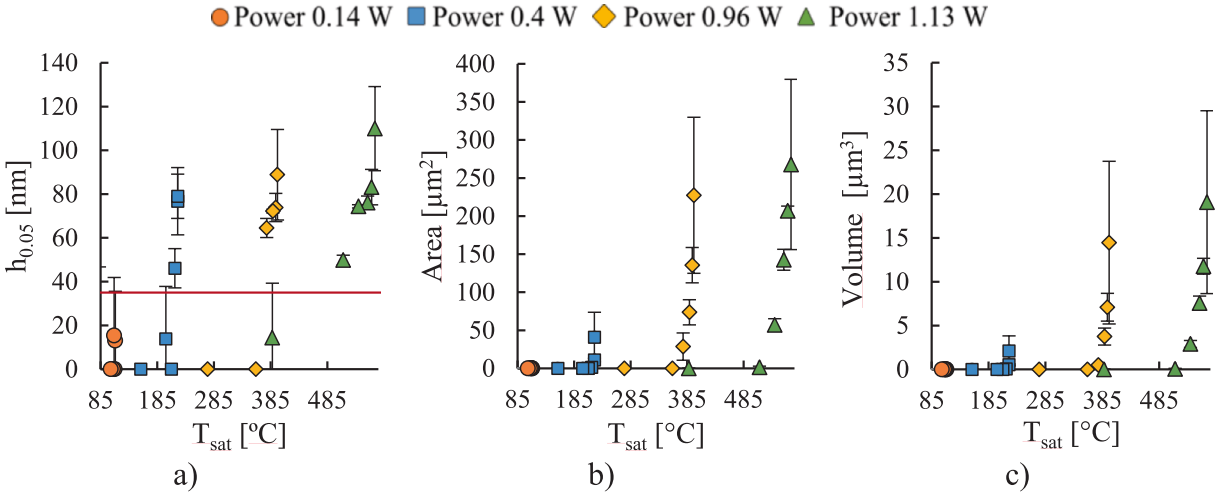

Fig. 5. Results for saturation temperature regarding burrs forming in lines. a) Height at the 5 % of the material area ratio, b) Projected area and c) Volume of the burrs.

present the results for the ablated lines, showing the height, area, and volume of the burr that formed on the lines, plotted against T_{sat}. Similar trends to those observed for dimples were evident, as the data clustered according to the applied level of laser power. Hence, a T_{sat} limit could be established for each power level. However, the T_{sat} limit for burr formation differed for dimples versus lines at each power level. At an average power of 0.4 W, burr formation in dimples was observed at $T_{sat} = 135$ °C. In contrast, for lines, the threshold was higher, at $T_{sat} = 216$ °C. These findings indicate that the T_{sat} limit does not depend solely on the applied laser power but is also influenced by the ablated geometry.

Comparing the results for dimples and lines, the burr area and volume for lines was consistently larger than that of dimples at the same power level, as expected (compare Fig. 4 (b) and (c) with Fig. 5 (b) and (c)). This difference was due to the larger laser-irradiated area in the case of lines. However, the burr height tended to be less for lines than dimples, with a maximum burr height of 209 nm for dimples and 109 nm for lines (compare Fig. 4 (a) with Fig. 5 (a)).

In summary, the T_{sat} limit for burr formation is influenced by both the applied average power and the geometry of the ablated structure. This dependency implies that T_{sat} cannot serve as a universal indicator for burr formation in models that evaluate different power levels. Separate experimental matrices are required for each power–geometry combination, which increases both the experimental complexity and the cost of determining the precise limits for burr formation.

4.2. Accumulated fluence

The performance of the proposed accumulated fluence as a burr indicator was evaluated. Fig. 6 (a), (b) and (c) present the results obtained for the height, area, and volume, respectively, of the burr of the dimples, plotted against the proposed novel indicator, F_{accu}. A correlation between the height of the burr and the F_{accu} value was evident and was independent of laser processing parameters. This finding differed from the power-level dependent results obtained for T_{sat}. Based on these results, three distinct regimes were identified: (i) no burr, (ii) burr initiation, and (iii) burr formation.

A no-burr regime occurred when $F_{accu} \leq 35$ J/cm^2. In this case, no burrs were observed, and all burr characterisation metrics remained at zero. For $35 \leq F_{accu} \leq 92$ J/cm^2, the burr-initiation regime was established. The burr height varied significantly, with large standard deviations and no clear trend (see Fig. 6a), whereas the burr area and volume remained close to zero (see Fig. 6b and 6c). When $F_{accu} \geq 92$ J/cm^2, burrs were formed, and their height increased linearly with accumulated fluence (see Fig. 6 (a)). The burr area and volume were clustered according to the power level (see Fig. 6 (b) and (c)). Area followed an exponential trend, whereas volume followed a linear trend. The clustering occurred because higher laser powers produce larger ablated diameters, which in turn increase the total perimeter of the dimple. Burrs form along the dimple edge, which means that a larger perimeter results in a larger burr area. Consequently, the burr volume also increases, as the expanded area is not fully offset by the linear rise in burr height. Thus, the clustering reflects the geometric effects of the ablated dimple that are introduced by varying power levels rather than a limitation of the proposed indicator. Additionally, in the burr-formation regime, burrs that formed under 1.13 W power had a larger standard deviation than those formed under 0.96 W.

Fig. 7 (a), (b) and (c) present the 3D and SEM measurements for dimples generated in the no-burr, burr-initiation and burr-formation regimes, respectively. Differences in the generated burr for each regime can be observed. Fig. 7 (d) and (e) illustrate a comparison of the height profiles and projected burr areas obtained for each burr-formation regime.

In the no-burr regime, no burrs were generated. This was confirmed by SEM analysis, as the edge of the dimple presented the same morphology as the reference surface material (Fig. 7 (a)). Additionally, all surface heights remained below the S_p of the reference surface (see Fig. 7 (d)) further verifying the absence of burrs. Consequently, burr-free dimples were achieved.

In the burr-initiation regime, SEM analysis (Fig. 7 (b)) revealed that the material surrounding the dimple exhibited subtle morphological differences compared to the reference surface. Only a non-uniform small amount of material exceeded the S_p value of the reference surface (Fig. 7 (d) and (e)). Additionally, there was no clear trend in burr height with increasing F_{accu}, and the standard deviations were large, with burrs being present in certain instances but absent in others. This was true even under identical processing conditions, as shown in Fig. 8. To further support these observations, statistical analyses were conducted. First, the standard deviations within the burr-initiation and burr-formation regimes were analysed through a Kruskal–Wallis test. The average standard deviation in the burr-initiation regime was 31.45 nm, compared to 21.6 nm in the burr-formation regime. The test revealed a

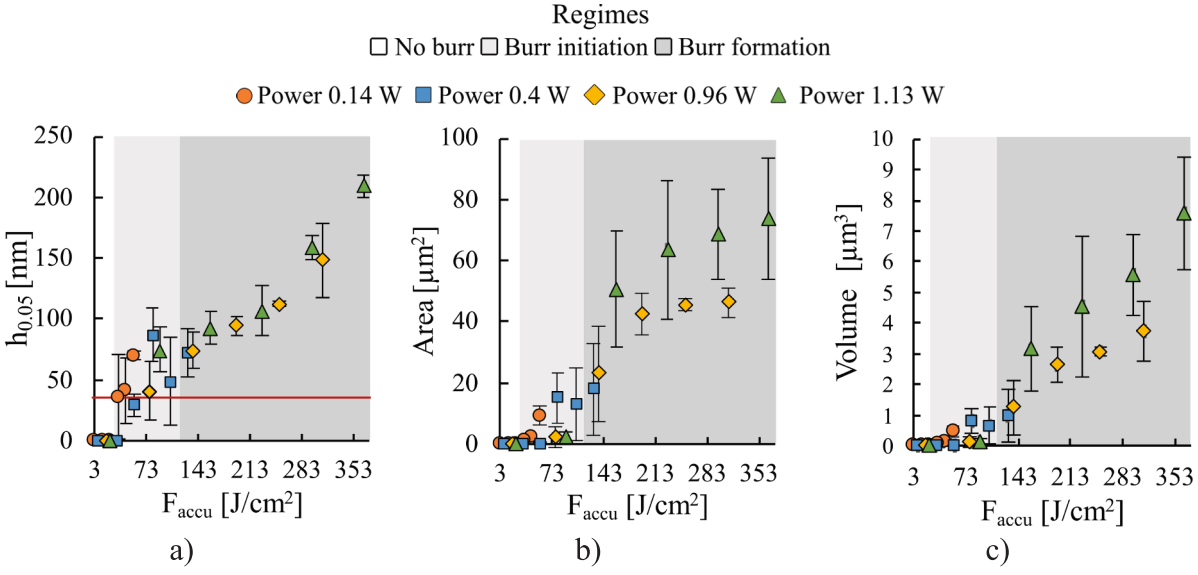

Fig. 6. Accumulated fluence results for the burr of the multi-shot dimple. a) Height at 5% of the material area ratio; the red line represents the S_p value of the reference surface. b) Projected area. c) Volume.

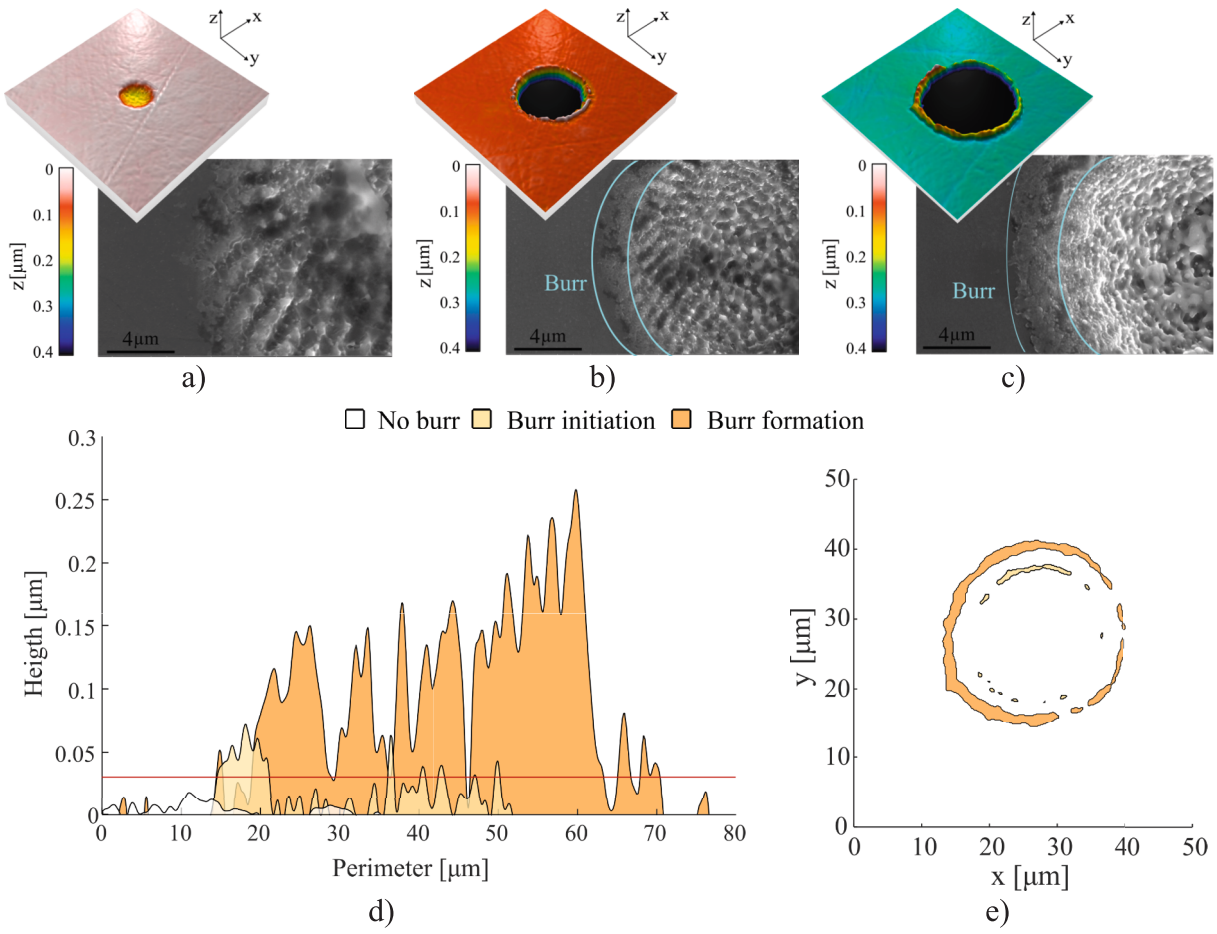

Fig. 7. SEM and 3D measurements of the burrs generated on the multi-shot ablated dimples. a) No-burr regime (Power = 0.14 W N_p = 10, F_{Accu} = 3.5 J/cm^2) b) Burr-initiation regime (Power = 0.4 W N_p = 100, F_{Accu} = 80.7 J/cm^2) and c) Burr-formation regime (Power = 1.13 W N_p = 160, F_{Accu} = 365 J/cm ^{2}) and comparison of the a) Height profile of the burrs. The red line indicates the S_p value of the reference surface and b) Projected area.

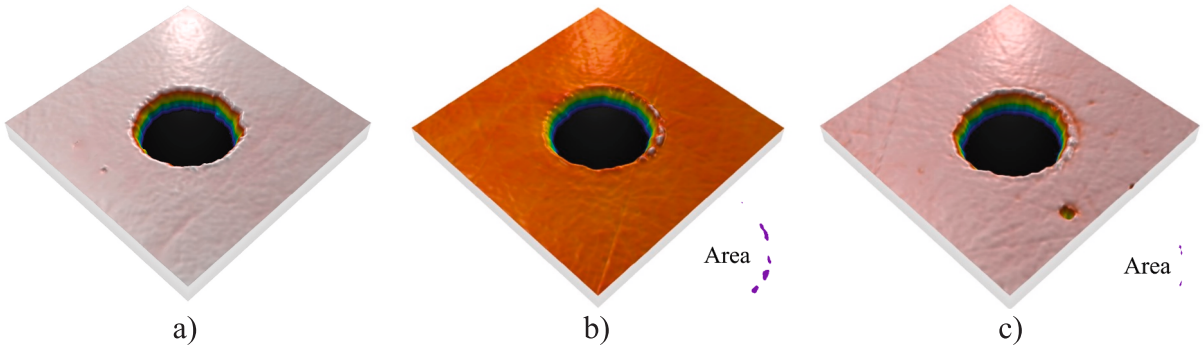

Fig. 8. 3D measurements of the generated burr of the multi-shot ablated dimple under 40 pulses and 0.96 W. a) First repetition; b) second repetition; and c) third repetition. The projected area of the burr is represented in purple.

statistically significant difference between the two groups, with a p-value of 0.03 (< 0.05), indicating that the burr-initiation regime exhibits significantly greater variability. Subsequently the relationship between burr height and F_{accu} within each regime was evaluated using a Spearman correlation analysis. The analysis revealed no statistically significant relationship between F_{accu} and burr height in the initiation regime as the Spearman correlation coefficient (r) was not close to 1 and the p-value was bigger than 0.05 (r = 0.357, p = 0.44). In contrast a strong, statistically significant correlation was found in the burr-formation regime (r = 0.9879, p < 0.001). These results reinforce the interpretation that burr formation in the initiation regime is stochastic in nature.

In the burr-formation regime, SEM analysis (Fig. 7 (c)) revealed a clear distinction between the dimple edge and the reference surface, which confirmed the formation of burrs. Nearly all burr height values exceeded the S_p of the reference surface (Fig. 7 (d)), indicating the presence of pronounced burr structures. Fig. 7 (e) illustrates the projected burr area, which extended almost continuously around the entire dimple perimeter in an asymmetric manner. The lack of symmetry is attributed to the stochastic nature of the burr formation process.

Additionally, an increase in the ablated dimple diameter was observed with increasing laser power, which correlates with the two data clusters that were evident for the generated burr area and volume (see Fig. 6 (b) and (c)).

Fig. 9 (a), (b) and (c) show the results obtained for the height, area, and volume of the burrs of the lines, respectively, as functions of F_{accu}. Similar to the results for dimples, a correlation was noted between burr characteristics and F_{accu}, independent of laser processing parameters. However, this time only two distinct regimes were identified: (i) no burr and (ii) burr formation. There was no intermediate burr-initiation regime as was the case for dimples. The larger irradiated area in line structures compared to dimples increases the probability of burr formation, which may lead to more consistent burr generation across many repetitions under the same processing conditions.

For $F_{accu} \leq 92$ J/cm^2, the no-burr regime was evident. Within this regime, no significant burr formation was observed; the $h_{0.05}$ values remained below the S_p threshold of the reference surface (see Fig. 9 (a)), while the burr area and volume remained close to zero (see Fig. 9 (b) and (c)). Burr formation commenced at $F_{accu} > 92$ J/cm^2, notably coinciding with the initiation of the burr-formation regime that was observed in dimples. However, despite sharing the same initiation threshold, the evolution of burr heights differed. A linear increase was observed in dimples (Fig. 6 (a)), whereas the lines exhibited behaviour that could be divided into two stages (Fig. 9 (a)). (i) The first stage was a constant burr-height region ($92 \leq F_{accu} \leq 253$ J/cm^2 range), where the burr height remained stable. (ii) The second stage was a linear burr-height increase region ($F_{accu} \geq 253$ J/cm^2), where the burr height exhibited a linear growth trend.

Also, in contrast to dimples, for lines the burr area and volume showed a continuous linear increase with increasing F_{accu}, without clustering by power level. This distinction occurs because in line geometries, the ablated width varies only slightly according to the power. Hence, it has minimal impact on the overall perimeter, which is primarily defined by the constant line length. Consequently, the total perimeter –and therefore the potential area for burr formation – remained almost constant across all the tested power levels. Under these conditions, no clustering was observed in the experimental results. This finding demonstrates that accumulated fluence can serve as a valid and power-independent indicator for burr formation.

Fig. 10 (a), (b), and (c) present the 3D and SEM measurements of lines generated in the no-burr regime, the constant burr-height region (L1 data point from Fig. 9 (a)), and the linear burr-height increase region of the burr-formation regime (L2 data point from Fig. 9 (a)), respectively. Fig. 10 (d) and (e) provide a comparative analysis of the height profiles and projected burr area.

In the no-burr regime, SEM analysis confirmed the absence of burr formation, as no discernible structures were observed along the line perimeter (Fig. 10 (a)). All height profiles remained below the S_p of the reference surface (Fig. 10 (d)), ensuring the generation of burr-free lines.

In the first region of the burr-formation regime ($92 \leq F_{accu} \leq 253$ J/cm^2 range), subtle differences were detected around the line edges, indicating burr formation (see Fig. 10 (b)). Material exceeding the S_p of the reference surface appeared as randomly distributed clusters along the line perimeter, indicating the stochastic nature of burr formation (see Fig. 10 (d)). These clusters formed predominantly along the edges of the lines, parallel to the scanning direction (Fig. 10 (e)). A comparison of points within this region (L1 and L3 in Fig. 9 (a)) revealed that while the burr height remained relatively constant (Fig. 11 (a)), the number of clusters increased (Fig. 11 (b)). This finding suggests that burr formation initially evolves over a maximal coverage area before further height development occurs.

In the second region of the burr-formation regime ($F_{accu} \geq 253$ J/cm^2), SEM analysis revealed a clear distinction between the line edges and the reference surface material (Fig. 10 (c)). The height profile of the burr significantly exceeded the S_p of the reference surface (Fig. 10 (d)). Compared to the first region, the burr distribution along the edges parallel to the scanning direction was more uniform (Fig. 10 (e)). This finding indicates that once the burr has fully formed along the parallel edges, further material accumulation will mainly increase the burr height. This would explain the different height growth in the two regions.

The absence of power-level clustering in the area and volume data is due to the concentration of the burr formation along the parallel edges. The line length was nearly constant across all laser processing parameters, which meant the available burr-forming perimeter remained unchanged. In contrast, in dimples, the irradiated area available for burr formation changed with the power level that was used. However, variations in burr formation were observed along the perpendicular edges of the lines. At the starting ablation point, no burr was detected, probably because the material was at room temperature with insufficient heat accumulated for burr formation. In contrast, at the end of the scan, a subtle burr was present, which probably indicated that preheating from

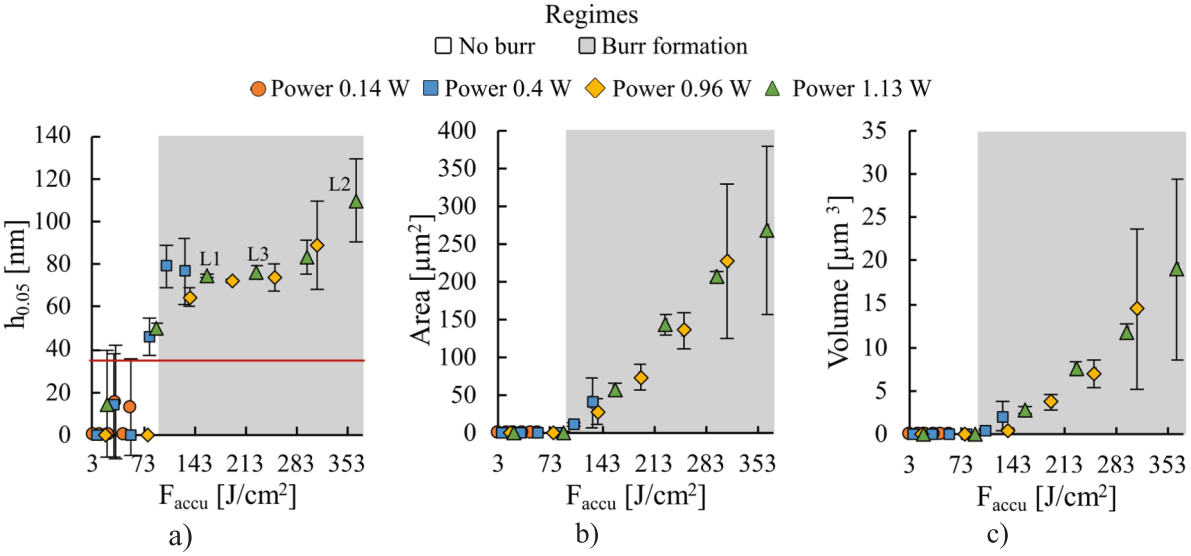

Fig. 9. Accumulated fluence results for the burr of the line. a) Height at the 5% of the material area ratio, where the red line represents the S_p value of the reference surface; b) projected area; and c) volume. L1 and L3 indicate the burrs that were analysed in the constant height region of the burr-formation regime. L2 is the burr that was analysed in the linear burr-height increase region of the burr-formation regime.

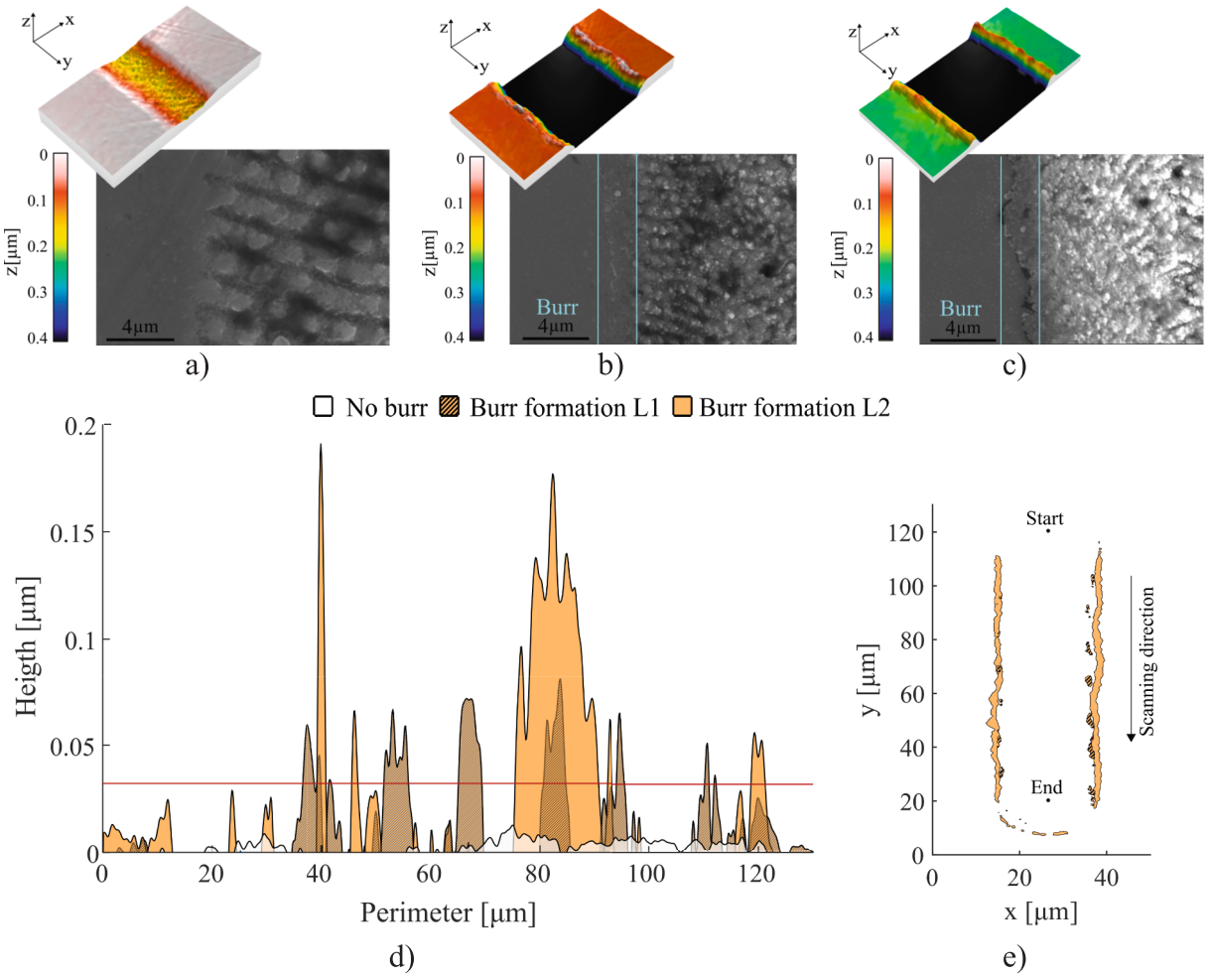

Fig. 10. The SEM and 3D measurements of burrs generated on the ablated lines. a) No-burr regime (power = 0.14 W, speed = 900 mm/s, and F_{Accu} = 3.5 J/cm^2). b) Burr-formation regime in the constant burr-height region (L1) (power = 1.13 W, speed = 129 mm/s, F_{Accu} = 160 J/cm^2). c) Burr formation regime in the linear height-increase region (L2) (power = 1.13 W, speed = 56 mm/s, F_{Accu} = 365 J/cm^2). Comparison of the d) Height profile of the burr. The red line indicates the S_p value of the reference surface and e) Projected area.

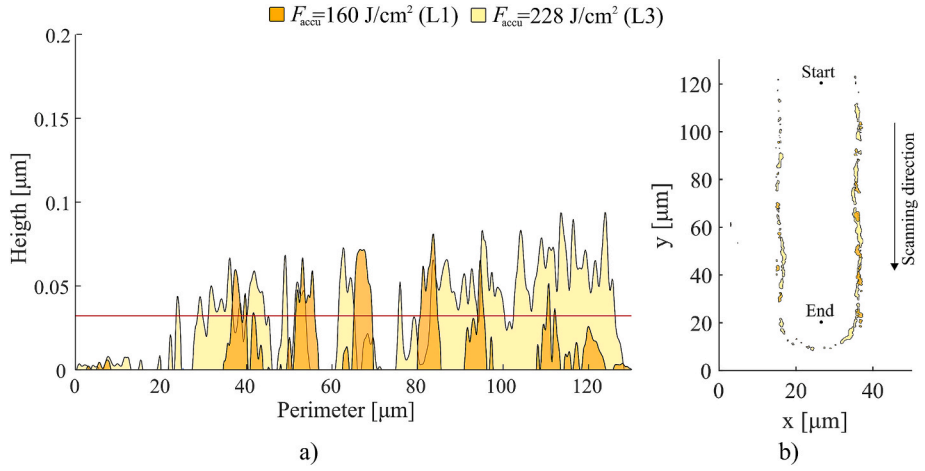

Fig. 11. Comparison between the burr formed in the constant burr-height region of the burr formation regime. a) Burr height profile and b) Projected area of L1 (Power = 1.13 W and Speed = 129 mm/sF_{accu} = 160J/cm^2) and L3 (Power = 1.13 W and Speed = 90 mm/sF_{accu} = 228J/cm^2) regions of the burr formation regime.

the preceding pulses had facilitated burr formation. It is worth noting that the acceleration and deceleration paths of the laser scanner probably also influence burr formation in the perpendicular edges. However, this effect was not considered in the present study.

Fig. 12 presents a comparison of the burr $h_{0.05}$ evolution with F_{accu} for dimples versus lines. The burr area and volume are significantly larger in lines than in dimples, due to the greater irradiated area in lines. Hence, the results in terms of projected area and volume are not

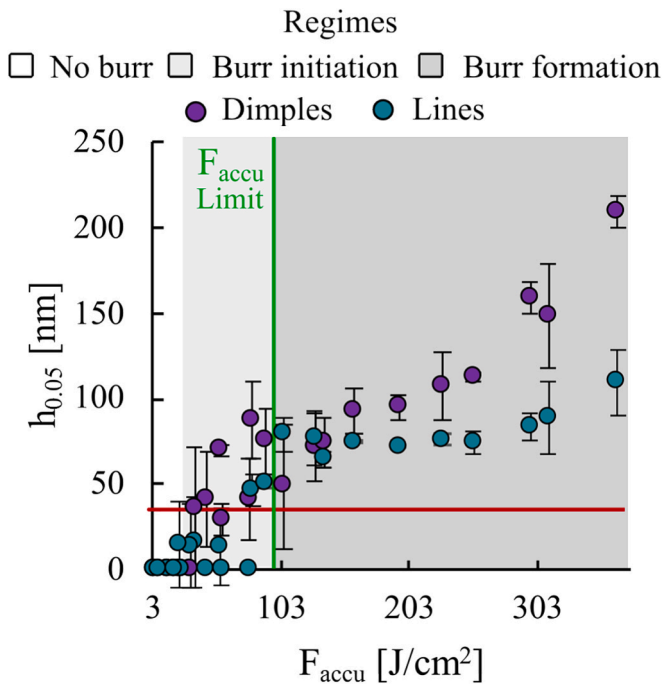

Fig. 12. Comparison of the burr height evolution for multi-shot dimples and lines. The red line indicates the Sp value of the reference surface. The green line indicates the F_{accu} threshold for the initiation of the burr-formation regime in both multi-shot dimples and lines.

comparable. The burr-formation regime consistently began at $F_{accu} = 92$ J/cm^2, in both geometries. However, three burr regimes were evident for dimples and only two were evident for lines. In lines, there was no burr-initiation regime, probably because the larger irradiated area increased the probability of consistently generating burrs. For dimples, in the burr-formation regime, the burr height increased linearly along with F_{accu}, whereas for lines, it remained constant up to $F_{accu} = 253$ J/cm^2, after which it began increasing linearly. In all cases, the burr height was greater for dimples than for lines (Fig. 12).

Overall, despite these differences in burr evolution, F_{accu} was a reliable predictor of burr formation. It enabled the efficient determination of burr-free processing limits, with minimal experimental effort. The results obtained for dimples can be extrapolated to lines, and the F_{accu} threshold for burr formation remains independent of the average power used. This finding confirms the universal relevance of F_{accu} as a key parameter to aid the selection of laser processing parameters to generate burr-free textures.

The F_{accu} limit also defines a maximum achievable depth for burr-free structuring under fixed processing conditions. To overcome this limitation, several strategies could be explored, such as adjusting parameters like the pulse repetition rate, which may increase the F_{accu} limit. Burst-mode ablation was not considered in this study but might enable deeper material removal by engaging alternative energy-deposition mechanisms. Additionally, only single-layer line ablation was investigated; it remains unclear whether fluence accumulates similarly across multiple layers. In multi-layer ablation, a relatively long interval between layer passes may mitigate the effects of heat accumulation, which could mean that applying the F_{accu} limit layer-by-layer could allow for the generation of deeper structures, without inducing burrs. While this approach increases the processing time, it offers a promising route for high-depth structuring. Further experimental studies are necessary to evaluate the validity and practical applicability of such strategies.

Further research is also required to check whether the F_{accu} limit depends on other process parameters, such as pulse duration or pulse repetition rate, which directly affect the heating and cooling behaviour between pulses which it is not considered in the current model. Additionally, to assess the universality of the F_{accu} limit, future studies should investigate a broader range of materials, such as titanium alloys and aluminium alloys. This would help clarify the influence of material-specific properties, such as thermal conductivity, reflectivity, and melting points, on burr-formation behaviour. Furthermore, in this study, burr formation was specifically explored as it is critical for tribological applications; however, for other applications, the surface functionality may be compromised by the degree of oxidation or resulting surface roughness. Hence, studying the relation between F_{accu} and these phenomena could provide valuable insights to determine whether limits can be established for such phenomena too.

5. Conclusion

Accumulated fluence (F_{accu}) was proposed and validated as an indicator for burr formation in multi-shot and line ablation which is independent of the average power used and the ablated geometry. This method minimises the experimental time and cost required to establish the limit for generating burr-free textures. The study also led to the following additional conclusions:

- The saturation temperature limit depends on both the average laser power and the ablated geometry, which means separate calibrations are required for each power level and geometry type. This complexity increases the experimental effort.
- This study provides a detailed and quantitative analysis of burr geometry (height, area, volume). The proposed method reduces sensitivity to measurement artifacts, particularly important when analysing nanoscale features, and offers a framework that can be adopted in future investigations, including those focused on the underlying physical mechanisms of heat accumulation.
- For multi-shot ablated dimples, three regimes were established to describe the burr evolution: (i) no burr, (ii) burr initiation, and (iii) burr formation. In the burr-formation regime, the height increased linearly with F_{accu}, whereas the area and volume displayed logarithmic and linear trends, respectively. Furthermore, the results clustered according to the power level, which was due to an increase in the ablated diameters.
- For line ablation, only two regimes were identified: (i) no burr and (ii) burr formation. In the burr-formation regime, the area and volume both increased linearly. The burr height remained constant until $F_{accu} = 253$ J/cm^2 was surpassed, after which it began to increase linearly.
- The burr formation evolved to maximise the area coverage before additional height began to develop.
- While the concept of accumulated fluence has previously been applied in contexts such as LIPSS formation, this work is the first to demonstrate its utility as a predictor for burr formation. The burr-formation regime for both multi-shot ablated dimples and lines commenced at the same accumulated fluence threshold of 92 J/cm^2, regardless of which power level was employed. Hence, the F_{accu} limit can be calibrated based on multi-shot dimples and then be extended to lines, despite differences in the burr evolution for dimples and lines.

Future work is necessary to assess whether the identified F_{accu} threshold is influenced by other laser processing parameters, such as pulse duration or pulse repetition rate. These can directly impact the heat accumulation between successive pulses but are not accounted for in the present model. Furthermore, to evaluate the universality of F_{accu} as an indicator for burr formation, future studies should investigate different metals, such as titanium or aluminium alloys. Additionally, while burr formation was the focus of this study due to its critical role in tribological applications, other functional surface properties, including oxidation and surface roughness, may be affected by different thermal

effects. Investigating the correlation between F_{accu} and these phenomena could provide valuable insights and help determine whether similar thresholds can be defined to ensure surface quality in a broad range of applications.

This study has presented F_{accu} as a novel and robust indicator of burr formation in femtosecond laser processing, with the indicator being independent of both geometry and power variables. Combined with the proposed burr characterisation methodology, the accumulated fluence indicator enables cost-effective calibration of burr-free laser processing windows, eliminating reliance on operator expertise for power and overlap control. It can also be integrated into laser parameter prediction models to optimise process design and facilitate the industrial adoption of femtosecond laser technology.

CRediT authorship contribution statement

Ainhoa Guinea: Writing – review & editing, Writing – original draft, Visualization, Software, Methodology, Investigation, Data curation. **Andrea Aginagalde:** Writing – review & editing, Supervision, Methodology, Investigation, Conceptualization. **Joseba Mendiguren:** Writing – review & editing, Resources, Formal analysis. **Eneko Saenz de Argandoña:** Writing – review & editing, Visualization, Formal analysis. **Aitor Ayerdi:** Writing – review & editing, Visualization, Formal analysis. **Wilson Tato:** Writing – review & editing, Formal analysis. **Alaitz Zabala:** Writing – review & editing, Writing – original draft, Supervision, Methodology, Investigation, Funding acquisition, Conceptualization.

Declaration of competing interest

The authors declare that they have no known competing financial interests or personal relationships that could have appeared to influence the work reported in this paper.

Funding

The authors gratefully acknowledge the financial support given by the Basque Government (Eusko Jaurlaritza) under the 'Programa de apoyo a la investigación colaborativa en áreas estratégicas' (Project FRONTIERS: Ref. KK-2024/00099), as well as the support received through a PhD fellowship from the Basque Government (Programa Predoctoral de Formación de Personal Investigador).

Data availability

Data will be made available on request.

References

[1] D. Gropper, L. Wang, T.J. Harvey, Hydrodynamic lubrication of textured surfaces: A review of modeling techniques and key findings, Tribol. Int. 94 (Feb. 2016) 509–529, https://doi.org/10.1016/j.triboint.2015.10.009.

[2] B. Dashtbozorg, et al., Development of surfaces with antibacterial durability through combined S phase plasma hardening and athermal femtosecond laser texturing, Appl. Surf. Sci. 565 (Nov. 2021), https://doi.org/10.1016/j.apsusc.2021.150594.

[3] K. Ding, C. Wang, S. Li, X. Zhang, N. Lin, J. Duan, Single-step femtosecond laser structuring of multifunctional colorful metal surface and its origin, Surf. Interfaces 34 (Nov. 2022), https://doi.org/10.1016/j.surfin.2022.102386.

[4] A. Orlandini, S. Baraldo, M. Porta, and A. Valente, "Ablation threshold estimation for femtosecond pulsed laser machining of AISI 316L," in *Procedia CIRP*, Elsevier B. V., 2022, pp. 617–622. doi: 10.1016/j.procir.2022.05.035.

[5] B. Kim, et al., Selective Laser Ablation of Metal Thin Films using Ultrashort Pulses, International Journal of Precision Engineering and Manufacturing - Green Technology 8 (3) (May 2021) 771–782, https://doi.org/10.1007/s40684-020-00272-w.

[6] A. Guinea, A. Aginagalde, J. Mendiguren, E. Saenz de Argandoña, I. Llavori, A. Zabala, Dimple prediction modelling in ultrashort laser processing: A benchmark study on ablation threshold determination methods and incubation models, Surf. Coat. Technol. 497 (Feb. 2025), https://doi.org/10.1016/j.surfcoat.2024.131712.

[7] G. Raciukaitis, M. Brikas, P. Gecys, and M. Gedvilas, "Accumulation effects in laser ablation of metals with high-repetition-rate lasers," in *High-Power Laser Ablation VII*, SPIE, May 2008, p. 70052L. doi: 10.1117/12.782937.

[8] F. Bauer, A. Michalowski, T. Kiedrowski, S. Nolte, Heat accumulation in ultra-short pulsed scanning laser ablation of metals, Opt. Express 23 (2) (Jan. 2015) 1035, https://doi.org/10.1364/oe.23.001035.

[9] B. Bornschlegel, J. Köller, J. Finger, In-situ analysis of heat accumulation during ultrashort pulsed laser ablation, Journal of Laser Micro Nanoengineering 15 (1) (Jun. 2020) 56–62, https://doi.org/10.2961/jlmn.2020.01.2010.

[10] J. Finger *et al.*, "Heat input and accumulation for ultrashort pulse processing with high average power," May 24, 2018, *Walter de Gruyter GmbH*. doi: 10.1515/aot-2018-0008.

[11] J. Martan, L. Prokešová, D. Moskal, B.C. Ferreira de Faria, M. Honner, V. Lang, Heat accumulation temperature measurement in ultrashort pulse laser micromachining, Int. J. Heat Mass Transf. 168 (Apr. 2021), https://doi.org/10.1016/j.ijheatmasstransfer.2020.120866.

[12] L. Cangueiro, J.A. Ramos-De-campos, D. Bruneel, Prediction of thermal damage upon ultrafast laser ablation of metals, Molecules 26 (21) (2021) Nov, https://doi.org/10.3390/molecules26216327.

[13] S. Shin, J.G. Hur, J.K. Park, D.H. Kim, Thermal damage free material processing using femtosecond laser pulses for fabricating fine metal masks: Influences of laser fluence and pulse repetition rate on processing quality, Opt. Laser Technol. 134 (Feb. 2021), https://doi.org/10.1016/j.optlastec.2020.106618.

[14] X. Jia *et al.*, "Ultrafast laser welding of transparent materials: from principles to applications," Jun. 01, 2025, *Institute of Physics*. doi: 10.1088/2631-7990/ada7a7.

[15] C. Lutz, M. Jung, K. Tschirpke, C. Esen, and R. Hellmann, "Optimization of Heat Accumulation during Femtosecond Laser Drilling Borehole Matrices by Using a Simplex Algorithm," *Materials*, vol. 15, no. 14, Jul. 2022, doi: 10.3390/ma15144829.

[16] A. Rahaman, A. Kar, X. Yu, Thermal effects of ultrafast laser interaction with polypropylene, Opt. Express 27 (4) (Feb. 2019) 5764, https://doi.org/10.1364/oe.27.005764.

[17] R. Weber, T. Graf, C. Freitag, A. Feuer, T. Kononenko, V.I. Konov, Processing constraints resulting from heat accumulation during pulsed and repetitive laser materials processing, Opt. Express 25 (4) (Feb. 2017) 3966, https://doi.org/10.1364/oe.25.003966.

[18] F. Nyenhuis, A. Michalowski, J. L'Huillier, Ultrashort pulse surface melting and smoothing: the impact of pulse spacing on heat accumulation and structure formation, J. Appl. Phys. 130 (5) (2021) Aug, https://doi.org/10.1063/5.0049987.

[19] S. Faas, U. Bielke, R. Weber, and T. Graf, "Prediction of the surface structures resulting from heat accumulation during processing with picosecond laser pulses at the average power of 420 W," *Appl Phys A Mater Sci Process*, vol. 124, no. 9, Sep. 2018, doi: 10.1007/s00339-018-2040-4.

[20] S. Shin, J.K. Park, D.-H. Kim, Suppression of spallation induced nanoparticles by high repetition rate femtosecond laser pulses: realization of precise laser material processing with high throughput, Opt. Express 29 (13) (Jun. 2021) 20545, https://doi.org/10.1364/oe.427168.

[21] R. Weber, et al., Heat accumulation during pulsed laser materials processing, Opt. Express 22 (9) (May 2014) 11312, https://doi.org/10.1364/oe.22.011312.

[22] J. Guo, T. Hu, Q. Li, Y. Liu, Nanosecond laser-induced dimple texturing of TB6 alloy surfaces: Tribological behavior under dry and starved-oil lubrication, Tribol. Int. 197 (Sep. 2024), https://doi.org/10.1016/j.triboint.2024.109842.

[23] J. Ma, Y. Liu, J. Mostaghimi, N. Zhang, Effect of laser preparation strategy on surface wettability and tribological properties under starved lubrication, Tribol. Int. 191 (Mar. 2024), https://doi.org/10.1016/j.triboint.2023.109107.

[24] J. Li, X. Wang, Numerical simulation of the influence of the bulges around laser surface textures on the tribological performance, Tribol. Trans. 56 (6) (2013) 1011–1018, https://doi.org/10.1080/10402004.2013.819956.

[25] T. Kar, S.S. Deshmukh, A. Goswami, Fabrication of micro holes using low power fiber laser: surface morphology, modeling and soft-computing based optimization, Adv. Manuf. (Dec. 2024), https://doi.org/10.1007/s40436-024-00484-2.

[26] H. Wei, C. Huang, H. Liu, D. Liu, P. Yao, D. Chu, Modeling and optimizing femtosecond laser process parameters for high-efficient and near damage-free micromachining of single-crystal GaN substrate, Mater. Sci. Semicond. Process. 153 (Jan. 2023), https://doi.org/10.1016/j.mssp.2022.107123.

[27] L. Omeñaca, S.M. Olaizola, A. Rodríguez, M. Gomez-Aranzadi, I. Ayerdi, E. Castaño, Experimental findings and 2 dimensional two-temperature model in the multi-pulse ultrafast laser ablation on stainless steel considering the incubation factor, Opt. Laser Technol. 180 (Jan. 2025), https://doi.org/10.1016/j.optlastec.2024.111507.

[28] E. Majchrzak, B. Mochnacki, Numerical simulation of thermal processes in a domain of thin metal film subjected to an ultrashort laser pulse, Materials 11 (11) (2018) Oct, https://doi.org/10.3390/ma11112116.

[29] M. Chijiiwa, N. Berger, M. Schäfer, P. Mitschang, and J. A. L'huillier, "The effect of temporal pulse overlaps to the morphology on stainless steel 304 at ps laser micro structuring".

[30] D. Holder, C. Hagenlocher, R. Weber, C. Röcker, M. Abdou Ahmed, and T. Graf, "Model for designing process strategies in ultrafast laser micromachining at high average powers," *Mater Des*, vol. 242, Jun. 2024, doi: 10.1016/j.matdes.2024.113007.

[31] D. Mikhaylov, T. Kiedrowski, A.F. Lasagni, Heat accumulation effects during ultrashort pulse laser ablation with spatially shaped beams, Journal of Laser Micro Nanoengineering 13 (2) (Sep. 2018) 95–99, https://doi.org/10.2961/jlmn.2018.02.0008.

[32] J. Eichstädt, G. R. B. E. Römer, and A. J. Huis In 'T Veld, "Determination of irradiation parameters for laser-induced periodic surface structures," *Appl Surf Sci*, vol. 264, pp. 79–87, Jan. 2013, doi: 10.1016/j.apsusc.2012.09.120.
[33] J. M. Liu, "Simple technique for measurements of pulsed Gaussian-beam spot sizes," 1982.
[34] P. Pawlus, R. Reizer, W. Żelasko, Characterization of the Maximum Height of a Surface Texture, Materials 16 (22) (2023) Nov, https://doi.org/10.3390/ma16227109.